INTERNATIONAL JOURNAL OF REFRIGERATION 69 (2016) 480–496

ELSEVIER

Available online at www.sciencedirect.com

ScienceDirect

journal homepage: www.elsevier.com/locate/ijrefrig

Dynamic and thermodynamic characteristics of the moving-coil linear compressor for the pulse tube cryocooler. Part A: Theoretical analyses and modeling

Haizheng Dang [a,*], *Lei Zhang* [a,b], *Jun Tan* [a,b]

[a] *National Laboratory for Infrared Physics, Shanghai Institute of Technical Physics, Chinese Academy of Sciences, 500 Yutian Road, Shanghai 200083, China*

[b] *University of Chinese Academy of Sciences, No.19A Yuquan Road, Beijing 100049, China*

ARTICLE INFO

Article history:
Available online 11 January 2016

Keywords:
Dynamic and thermodynamic characteristics
Moving-coil linear compressor
Stirling-type pulse tube cryocooler
Theoretical analyses and modeling

ABSTRACT

Theoretical analyses and modeling are conducted on dynamic and thermodynamic characteristics of the moving-coil linear compressor in the Stirling-type pulse tube cryocooler. Governing equations are deduced, and φ and ΔP are found to be the two key parameters connecting compressor to pulse tube cold finger. An improved ECA model is developed to investigate the cold finger characteristics and their influences on φ, ΔP. Systematic simulations based on a specific case are performed to provide elaborate explanations about the theoretical analyses with the frequency varying from 30 Hz to 100 Hz at 60 K, 80 K and 100 K, respectively. The variations of four important parameters of φ, ΔP, I and θ, and the compressor thermodynamic performances and the cryocooler cooling performances, with the frequency at above temperatures are simulated and analyzed, respectively. The effects of compressor geometrical parameters on η_{motor} are also simulated. The experimental verifications will be presented in Part B.

Caractéristiques dynamique et thermodynamique du compresseur linéaire à serpentin mobile pour cryorefroidisseur à tube à pulsation Partie A: Analyses théoriques et modélisation

Mots clés : Caractéristiques dynamique et thermodynamique ; Compresseur linéaire à serpentin mobile ; Cryorefroidisseur à tube à pulsation de type Stirling ; Analyses théoriques et modélisation

* *Corresponding author.* National Laboratory for Infrared Physics, Shanghai Institute of Technical Physics, Chinese Academy of Sciences, 500 Yutian Road, Shanghai 200083, China. Tel.: +86 21 25051967; Fax: +86 21 65830734.
E-mail address: haizheng.dang@mail.sitp.ac.cn (H. Dang).
http://dx.doi.org/10.1016/j.ijrefrig.2015.12.019

Nomenclature

A	cross section area
B	magnetic field in air gap
c	damping coefficient
C	hydraulic capacity
D	diameter of piston
f	operating frequency
$\bar{F}$	motor force
$\bar{F_i}$	inertia force
$\bar{F_g}$	gas force
$\overline{F_m}$	mechanical spring force
$\overline{F_{vd}}$	viscous dissipation
$\bar{F_b}$	gas force on the backside of the piston
i	input current
I	amplitude of input current
k_m	axial stiffness of flexure spring
L_e	inductance of coil wire
L	length of wire in coil
l	length of each component
m	moving mass
$\Delta\dot{m}$	amplitude of mass flow rate
ΔP	amplitude of the dynamic pressure in the compression space
P	dynamic pressure
P_m	charge pressure
$\langle\dot{Q}_h\rangle$	time-averaged joule loss
$\langle\dot{Q}_c\rangle$	cooling capacity
r	ideal gas constant
R	resistance of coil wire
t	time
T	temperature of each component
u	input voltage
U	amplitude of input voltage
$\Delta\dot{U}$	amplitude of volume flow rate
V	volume
$\langle\dot{W}_e\rangle$	time-averaged electric power of the compressor
$\langle\dot{W}_{motor}\rangle$	time-averaged motor power
$\langle\dot{W}_{PV}\rangle$	time-averaged compressor PV power
x	displacement of piston
X	amplitude of piston's displacement
Z	hydraulic impedance

Greek symbols

α	phase angle between dynamic pressure and volume flow rate in compression space
θ	phase angle between position of piston and the input current
τ	operating period
φ	phase angle between displacement and dynamic pressure in compression space
η_{motor}	conversion efficiency of compressor from electrical to motor power
η_{pv}	conversion efficiency of compressor from electrical to acoustic power
η_{Carnot}	relative Carnot efficiency of the SPTC
γ	ratio of specific heat
ω	angular frequency
μ	dynamical viscosity
ψ	phase angle between input current and voltage
ρ	density of the working gas

Subscripts

IT	inertance tube
PT	pulse tube
reg	regenerator
r	reservoir
com	compressor
p	piston

1. Introduction

The past three decades have witnessed a worldwide quest for the space-qualified Stirling-type pulse tube cryocooler (SPTC) (Nguyen et al., 2014; Raab and Tward, 2010; Ross, 2007; Ross and Boyle, 2007). Most space SPTCs are driven by the Oxford-type linear compressor based on the well-proven principles that feature the clearance seal and flexure springs (Bailey et al., 2001, 2010–2011; Davey, 1990; Marquardt et al., 1993). Of the three types of linear compressors, namely, moving-iron, moving-coil, and moving-magnet ones, the moving-coil design avoids open circuit axial forces and torques on the current carrying coil and is much easier to completely eliminate the radial forces. Due to the proven high efficiency, low EMI noise, enhanced reliability and manufacturability, the Oxford-type moving-coil linear compressor has served as the principal driver for driving space SPTCs in practical space missions (Bailey et al., 2001, 2010–2011; Dang, 2015; Davey, 1990; Marquardt et al., 1993; Nguyen et al., 2014; Raab and Tward, 2010; Ross, 2007; Ross and Boyle, 2007).

Fig. 1 shows a schematic of a typical moving-coil linear compressor developed in the authors' laboratory. It employs the balanced-opposed arrangement to minimize the self-induced vibrations from the two halves, each of which comprises a cylinder, a piston with a shaft, two sets of flexure springs, a position transducer, a pressure vessel, and a linear motor composed of a permanent magnet, a moving coil and two return irons. Each coil is firmly fastened to the respective piston shaft, while each piston is radially supported by the two sets of flexure springs, which are parallel to each other and both are rigidly connected to the piston shaft. During the operation each piston is driven by the respective motor and reciprocates in its own cylinder. Two position transducers are fixed on the corresponding piston shafts, respectively, to closely monitor the respective movements of the pistons. It should be noted that the motors shown in Fig. 1 adopt the geometry of radial magnet with long coil. In practice, there are also three other types of geometries, viz. axial magnet with long coil, axial magnet with short coil, and radial magnet with short coil (Dang, 2015). The discussions and conclusions in this paper are universally applicable to all of the four types of motor geometries.

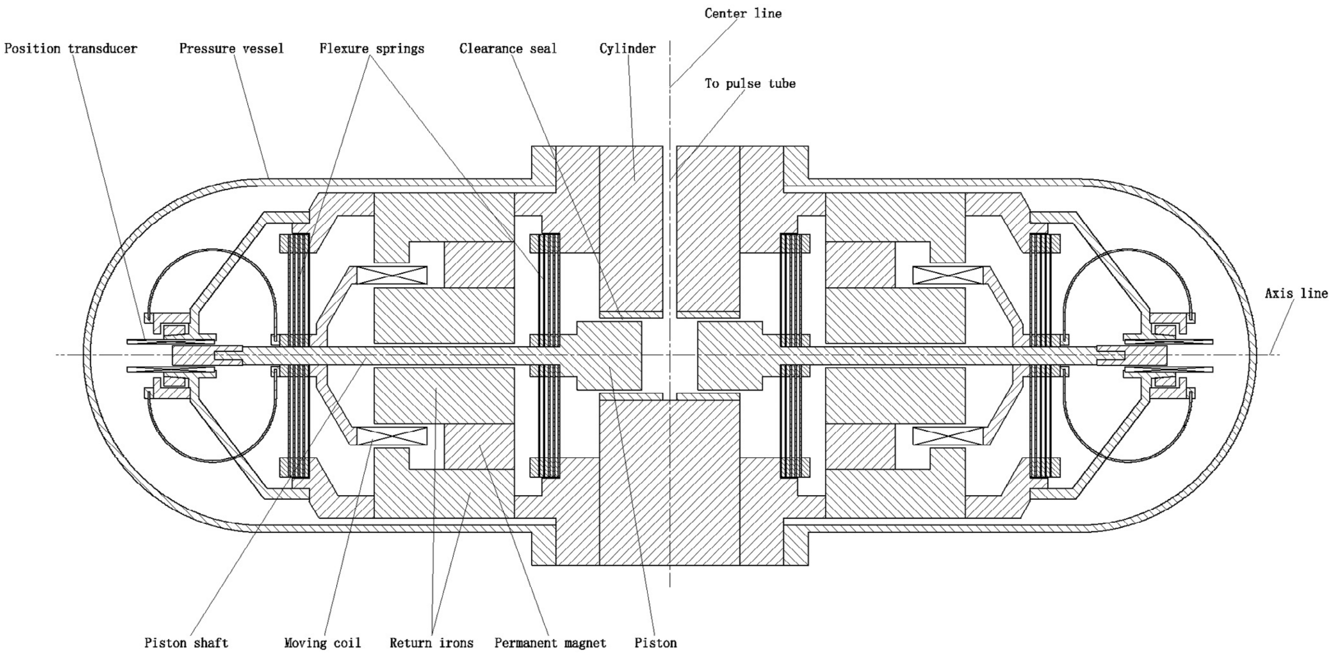

Fig. 1 – Schematic of a typical Oxford-type moving-coil linear compressor.

Phase characterization plays a vital role in the performance improvement of an SPTC. The inertance tube, due to its simple configuration, powerful phase-shifting ability, especially considering its complete passivity, has been widely employed as an effective phase-shifting approach in developing reliable and efficient SPTCs for space applications. In addition, based on the geometrical arrangements of the cold finger, the SPTC can also be divided into three types: U-type, coaxial and in-line. The following analyses and modeling are mainly based on the three types of SPTCs with the inertance tube as the phase-shifter.

2. Dynamic and thermodynamic characteristics of the linear compressor

2.1. *Previous studies survey*

The linear compressor has been studied widely (Bradshaw et al., 2011; Kim et al., 2009; Kim and Jeong, 2014; Ko and Jeong, 2008; Ko et al., 2008; Liang et al., 2014; Marquardt et al., 1993). However, in the field of cryogenics, few studies have been done on the dynamic and thermodynamic characteristics of the compressors, especially when coupled with the pulse tube cold fingers. The key dynamic parameters mainly include the input current, the operating frequency, the stroke, and the forces on the piston, while the thermodynamic parameters mainly consist of the dynamic pressure and the volume flow rate in the compression space, and also the phase angle between the dynamic pressure and the displacement. The gas force on the piston connects the two kinds of parameters, both of which exert important effects on the compressor performance.

Marquardt et al. (1993) derived a set of governing equations used to design the various components in the Oxford-type compressor, and further developed the scaling laws for it covering a wide range of sizes from 3 watts to 4 kilowatts. The equations and scaling laws dealt with the dynamic and thermodynamic characteristics of a linear compressor, but the cases when the cold fingers were coupled were not discussed. Gaunekar et al. (1994) made a dynamic and thermodynamic analysis on the double coil linear motors for a miniature Stirling cryocooler, and gave the governing equations of the current and input power through Fourier analysis, but their experiments caused a non-sinusoidal behavior and complicated the analyses. Yuan et al. (1994) predicted the natural frequency of an 80 K Stirling cryocooler and concluded that the piston diameter had the biggest impact on it and the effective way of adjusting the frequency was to change the moving mass. Heun et al. (1997) investigated the effect of working fluid on the dynamic characteristics of the Stirling cooler, in which both the stroke amplitude and the phase response of the cooler were examined and found that pneumatic effects had a significant impact on the cooler resonance characteristics. Koh et al. (2002) studied the characteristics of the linear compressor for the Stirling and experimentally found that both operating frequency and charge pressure had significant effects to the compressor performance. Ko and Jeong (2008) made the analysis about the SPTC and found that the dynamic behavior of the piston was directly influenced by the load. Ko et al. (2008) further made experimental investigations on the dynamic behavior and found that the thermodynamic characteristics and the cooling performance of a SPTC were governed by the dynamic behavior of a piston as well as the cooler configuration. Ki and Jeong (2012) discussed the design methodology for the efficient SPTC, in which both compressor and cold finger were suggested to be designed and optimized in consideration of each other.

As discussed in the above survey, in terms of the dynamic and thermodynamic characteristics of the linear compressor for the SPTC, most of the previous studies mainly paid attention to the governing equations of the linear compressor itself. A few studies theoretically discussed or experimentally tested the effects of the cold finger on the compressor, but systematic analyses and experimental verifications have not been carried out. In view of the above deficiencies, these characteristics will be investigated theoretically in this paper as follows:

(1) The governing equations of the dynamic and thermodynamic characteristics based on the Oxford-type moving-coil linear compressor will be deduced, and the key parameters which connect the compressor to the pulse tube cold finger will be determined.
(2) A further improved electric circuit analogy (ECA) model about the inertance tube SPTC will be built, and then the theoretical modeling will be conducted to investigate the thermodynamic characteristics of the cold finger and their influences on the key parameters acquired in the preceding step.
(3) Based on the above governing equations and theoretical modeling, the thermodynamic performances of the linear compressor and of the whole SPTC will be analyzed.
(4) Systematic simulations on a specific case will be carried out to provide elaborate explanations about the abovementioned theoretical analyses and the proposed model.

2.2. *Governing equations of dynamic and thermodynamic characteristics*

During the operation, there are mainly the following six forces exerted on the piston: the linear motor force $\vec{F}$, the inertial force $\vec{F_i}$, the mechanical spring force $\vec{F_m}$, the gas force $\vec{F_g}$, the viscous dissipation $\vec{F_{vd}}$, and the force $\vec{F_b}$ caused by the dynamic pressure on the backside of the piston (Marquardt et al., 1993). For most practical compressors, the volume of the gas on the backside of the piston is much larger than that of the compression space, which means $\vec{F_b}$ is negligible compared with other forces. So the remaining five forces form the balance, as shown in Fig. 2. The characteristics of a linear compressor are represented by Eq. (1) and Eq. (2) (Marquardt et al., 1993):

$$\vec{F} = \vec{F_i} + \vec{F_{vd}} + \vec{F_m} + \vec{F_g} \tag{1}$$

$$BiL = m\frac{d^2x}{dt^2} + c\frac{dx}{dt} + k_m x + (P - P_m)A_p \tag{2}$$

where i is the input current, L is the length of the wire in the coil, m is the moving mass, c is the damping coefficient, x is the displacement of the piston, k_m is the axial stiffness of the flexure springs, P is the dynamic pressure in the cylinder, and A_p is the cross area of the piston. We have:

$$i = I\sin(\omega t + \theta) \tag{3}$$

$$x = X\sin(\omega t) \tag{4}$$

$$P = P_m + \Delta P\sin(\omega t + \varphi) \tag{5}$$

where θ is the phase angle between the position of the piston and the input current, and φ is the phase angle between the displacement of the piston and the dynamic pressure.

The above five forces are determined by (Marquardt et al., 1993):

$$|\vec{F}| = BIL \tag{6}$$

$$|\vec{F_i}| = \omega^2 mX \tag{7}$$

$$|\vec{F_{vd}}| = c\omega X \tag{8}$$

$$|\vec{F_g}| = \Delta P A_p \tag{9}$$

$$|\vec{F_m}| = k_m X \tag{10}$$

According to above equations, the force balance on the piston can be expressed by Eq. (11) and Eq. (12), as shown in Fig. 2.

$$|\vec{F}|\cos\theta + |\vec{F_i}| = |\vec{F_m}| + |\vec{F_g}|\cos\varphi \tag{11}$$

$$|\vec{F}|\sin\theta = |\vec{F_{vd}}| + |\vec{F_g}|\sin\varphi \tag{12}$$

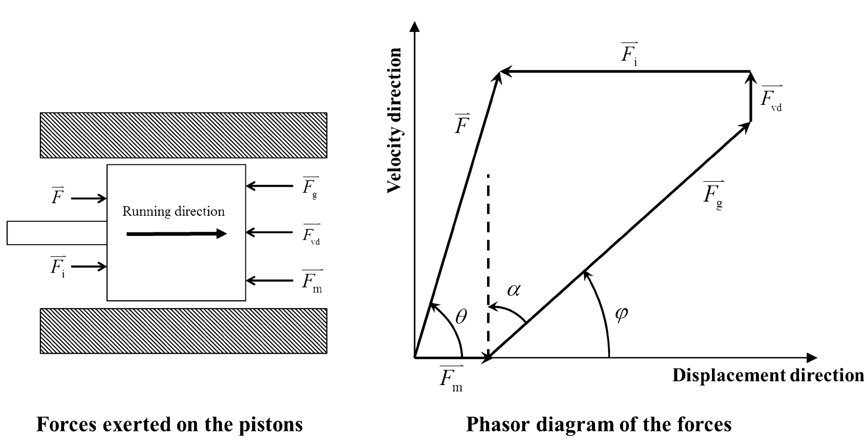

Fig. 2 – Forces exerted on the pistons.

Substituting Eqs. (6) through (10) into Eq. (11) and Eq. (12) yields:

$$BIL\cos\theta + \omega^2 mX = k_m X + \Delta P A_p \cos\varphi \tag{13}$$

$$BIL\sin\theta = \omega c X + \Delta P A_p \sin\varphi \tag{14}$$

In the above two equations, the following seven parameters can be provided artificially:

(1) The moving mass m;
(2) The magnetic field B;
(3) The wire length L;
(4) The axial mechanic springs stiffness k_m;
(5) The piston cross sectional area A_p;
(6) The angle frequency ω;
(7) The piston stroke X.

The remaining four parameters, viz. φ, ΔP, I and θ will vary with ω and X, respectively. However, the four unknown parameters cannot be determined by two equations. More equations have to be supplemented.

The compression space serves as both the exit of the compressor and the inlet of the pulse tube cold finger. Therefore, φ and ΔP are also the inlet characteristics of the working gas in the cold finger, which become the key parameters connecting the compressor to the cold finger. The two parameters subsequently depend strongly on the thermodynamic characteristics of the cold finger. Hence, the influence of the cold finger on the thermodynamic characteristic of the gas in the compression space must be studied. In the following section, the theoretical modeling of the SPTC will be conducted based on an improved ECA model.

3. Theoretical modeling of the pulse tube cryocooler with the electrical circuit analogy

In the ECA, the dynamic pressure and the volume flow rate are analogized to the voltage and the current, respectively, and thus the components consist of the hydraulic resistances, hydraulic capacities and hydraulic inductances. The thermodynamic characteristics at any position of the cold finger can be determined and then the influences of the cold finger on the linear compressor can be defined.

A variety of ECA models were ever proposed (Bailly and Nika, 2002; David and Marechal, 1995; Nika and Bailly, 2002; Storch et al., 1990; Swift, 2002); however, they are mainly used to optimize the inertance tube and to analyze the crude phase of dynamic pressure and the volume flow rate, whereas the specific analyses and optimizations of other components or the whole SPTC have not been made. Recently, Tan and Dang (2015) proposed a new ECA model including the main components of SPTC except heat exchangers, in which the calculation expressions of the components were worked out and their equivalent analogical electrical elements were defined, and the specific pressure and volume flow rate at any position could be acquired. However, in the model, both the amplitude of the dynamic pressure and the volume flow rate at the inlet of the cold finger must be defined in advance, and then the thermodynamic characteristics of the working gas in each component are calculated in the following order: First, in the regenerator; second, in the pulse tube; and finally, in the phase shifter. By contrast, for the present study, according to Section 2.2, the dynamic pressure at the inlet of the cold finger is the very object to be determined, and thus the model does not apply to the case. In addition, in the model (Tan and Dang, 2015), the effect of the compression space of the cylinder on the thermodynamic characteristics of the compressor was also ignored, which also plays a key role in the case of the present study. Therefore, to make thorough and accurate analyses of the effect of a pulse tube cold finger on the compressor, a further improved ECA model, as shown in Fig. 3(a) and (b), has to be developed, and the governing equation of each component will be deduced from the very beginning. The model contains all of the components of the model proposed by Tan and Dang (2015), plus three heat exchangers and the compression space. Furthermore, the calculation of the thermodynamic characteristics will start from the phase shifter, and only one parameter needs to be assumed in advance.

In an ideal gas reservoir, the dynamic pressure can be neglected. Therefore, when $\Delta\widetilde{U}_5$ at the inlet of the inertance tube is given, $\Delta\tilde{P}_5$ can be acquired. Based on the results, $\Delta\widetilde{P}_4$ and $\Delta\widetilde{U}_4$ at the inlet of Warm HX II can be calculated, and then the amplitudes of the dynamic pressure and the volume flow rate at the inlets or exits of all the remaining components can also be calculated in proper order. Finally, the thermodynamic characteristics in the compression space of the linear compressor can be determined. The detailed deduction process of each component will be given as follows.

3.1. Phase shifter

Based on the analogy of an electrical system, the complex impedance at inlet of the inertance tube can be expressed by (Lewis et al., 2006; Magnusson, Boston; Skilling, 1951):

$$Z_{IT} = Z_0\left[\frac{Z_r + Z_0\tanh(Kl_{IT})}{Z_0 + Z_r\tanh(Kl_{IT})}\right] \tag{15}$$

where Z_0, K, Z_r are the complex characteristic impedance, the complex propagation function and the impedance of the reservoir, respectively, and can be expressed as follows (Magnusson, Boston; Skilling, 1951):

$$Z_0 = \sqrt{[r(D) + i\omega l(D)]/[i\omega c(D)]} \tag{16}$$

$$K = \sqrt{[r(D) + i\omega l(D)]i\omega c(D)} \tag{17}$$

$$Z_r = \frac{\gamma r T_r}{i\omega V_r} \tag{18}$$

where $r(D)$, $l(D)$, $c(D)$ are the resistance, the inertance, and the compliance per unit length of the fluid in the inertance tube, respectively, and can further be expressed as follows (Lewis et al., 2006):

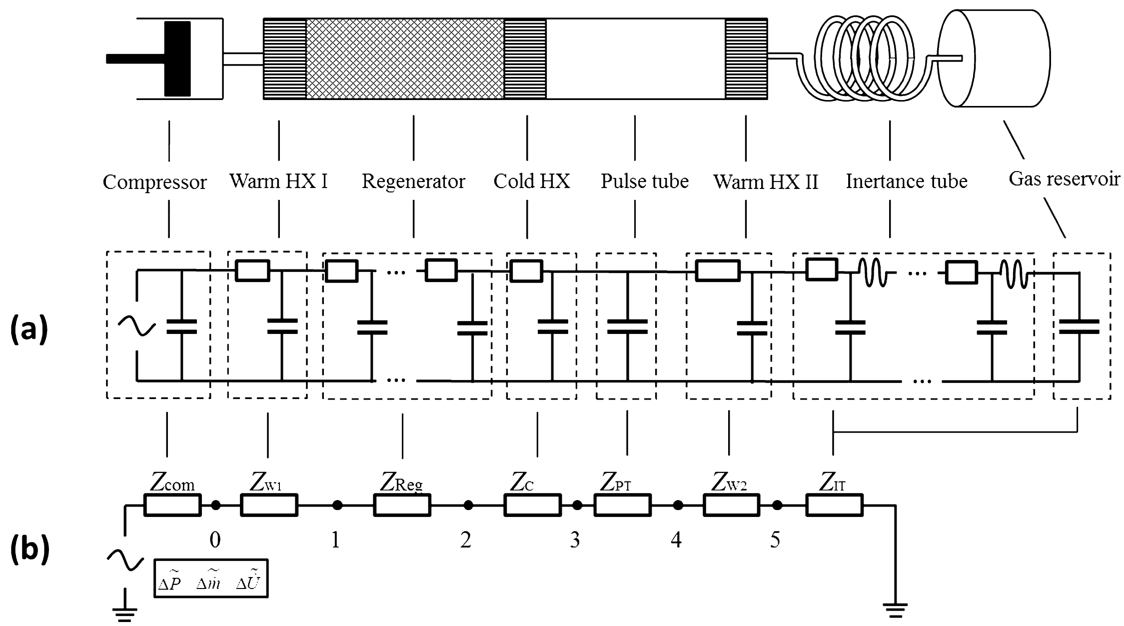

Fig. 3 – Theoretical model of the SPTC with an electrical circuit analogy.

$$r(D)=\frac{64 f_r |\Delta\widetilde{m}_5|}{\pi^3 \rho D^5} \tag{19}$$

$$l(D)=\frac{4}{\pi D^2} \tag{20}$$

$$c(D)=\frac{\pi D^2}{4\gamma r T} \tag{21}$$

Therefore, the dynamic pressure at the inlet is given by:

$$\Delta\widetilde{P}_5=\Delta\widetilde{m}_5 Z_{IT} \tag{22}$$

The mass flow rate in either Eq. (19) or Eq. (22) is given by:

$$\Delta\widetilde{m}_5=\rho_5 \Delta\widetilde{U}_5 \tag{23}$$

where ρ_5 is the average densities of the gas in the inertance tube and can be expressed as:

$$\rho_5=\frac{P_m}{rT_5} \tag{24}$$

In the authors' laboratory, the double-segmented inertance tube with different inner diameters and lengths, respectively, has usually been adopted as the main type of phase shifters (Dang, 2014, 2015). Based on Eqs. (15) through (21), the impedance Z_{IT1} at the inlet of the inertance tube next to the reservoir can be determined. To calculate the impedance Z_{IT2} at the inlet of the other inertance tube, Z_r in Eq. (15) should be replaced by Z_{IT1}, and then:

$$Z_{IT2}=Z_0\left[\frac{Z_{IT1}+Z_{0,2}\tanh(K_2 l_{IT2})}{Z_{0,2}+Z_{IT1}\tanh(K_2 l_{IT2})}\right] \tag{25}$$

Based on the assumed volume flow rate at the inlet of the inertance tube IT2, the impedance and the dynamic pressure of the phase shifter can be determined.

3.2. *Pulse tube*

The gas in the pulse tube can be virtually divided into three segments along the axial direction, and the middle one is regarded as the gas displacer. The working gas forms a temperature gradient along the axial direction. The gas density is determined by the temperature and thus varies with the position of gas. Thus the gas mass in the pulse tube is not conserved during the operation, but the gas volume is still conserved. So the gas flow in the pulse tube can be analyzed by the conservation of the gas volume.

For an ideal pulse tube, the pressure can be regarded as constant along the axial direction, and thus:

$$\Delta\widetilde{P}_3=\Delta\widetilde{P}_4 \tag{26}$$

So the resistance and the inertance of the pulse tube can be neglected, and only the hydraulic capacity C_{PT} exerts an effect on the gas, which can be expressed as:

$$C_{PT}=\frac{V_{PT}}{\gamma P_m} \tag{27}$$

Therefore, the volume flow rate at the inlet of the pulse tube is given by:

$$\Delta\widetilde{U}_3 - \Delta\widetilde{U}_4 = i\omega C_{PT}\Delta\widetilde{P}_3 \tag{28}$$

$$\Delta\widetilde{U}_3 = \Delta\widetilde{U}_4 + \frac{i\omega V_{PT}}{\gamma P_m}\Delta\widetilde{P}_3 \tag{29}$$

3.3. Regenerator

The working gas in the regenerator also has an axial temperature gradient and can also be analyzed by the conservation of the gas volume. The inductance of the regenerator can be neglected compared with its resistance owing to the ratio of its length to diameter. Thus the impedance of the regenerator consists of the resistance, the capacity and the thermally induced volume-flow-rate source (Swift, 2002). Based on the continuity and momentum equations, we have:

$$\Delta\widetilde{P}_x - \Delta\widetilde{P}_2 = \int_0^x r_g \Delta\widetilde{U}_x dx \tag{30}$$

$$\Delta\widetilde{U}_x - \Delta\widetilde{U}_2 = \int_0^x \left(c_g \Delta\widetilde{P}_x + g\Delta\widetilde{U}_x\right) dx \tag{31}$$

where x is the distance between the current position and the exit of the regenerator, and r_g and c_g are given by (Bailly and Nika, 2002; Nika and Bailly, 2002; Swift, 2002):

$$r_g = \frac{\mu}{2\varepsilon d_h^2 A_{reg}}(a + b\,Re) \tag{32}$$

$$c_g = i\omega \frac{\varepsilon \pi D^2}{4\gamma P_m} \tag{33}$$

where a and b are the specific coefficients to calculate r_g and can be determined by experiments (Bailly and Nika, 2002).

In Eq. (31), g is the coefficient of the controlled source term in the ECA model (Swift, 2002):

$$g = \frac{2(T_1 - T_2)}{l_{reg}(T_1 + T_2)} \tag{34}$$

Specific expressions of the dynamic pressure and the volume flow rate are given in Appendix A.

3.4. Heat exchangers

Based on ideal assumptions, all of the three heat exchangers, Warm HX I, Cold HX, and Warm HX II, shown in Fig. 3, are isothermal, and furthermore, the inductances of the heat exchangers can also be neglected. Therefore, the relationships between the gas at the inlet and exit of each heat exchanger can be expressed as:

$$\Delta\widetilde{P}_{in} - \Delta\widetilde{P}_{out} = \int_0^{l_{HX}} r_{HX} \Delta\widetilde{U}_x dx \tag{35}$$

$$\Delta\widetilde{U}_{in} - \Delta\widetilde{U}_{out} = \int_0^{l_{HX}} i\omega \frac{A_{HX}}{\gamma P_m}\Delta\widetilde{P}_x dx \tag{36}$$

where r_{HX}, A_{HX} are the resistance per unit length and the valid cross area of the heat exchanger, respectively.

3.5. Compression space

Both resistance and inductance of the compression space can be neglected compared with the capacity owing to the ratio of its length to diameter. Therefore, the dynamic pressure at the piston surface is equal to the pressure at the inlet of the regenerator:

$$\Delta\tilde{P} = \Delta\widetilde{P}_0 \tag{37}$$

The average hydraulic capacity of the compression space is given by:

$$C_{com} = i\omega \frac{V_{com}}{\gamma P_m} \tag{38}$$

where V_{com} is the volume of the compressor space when the piston arrives at the intermediate position.

The volume follow at the surface of the piston can be expressed as:

$$\Delta\tilde{\tilde{U}} = \Delta\widetilde{U}_0 + i\omega \frac{V_{com}}{\gamma P_m}\Delta\widetilde{P}_0 \tag{39}$$

According to Eqs. (37) and (39), the impedance of the SPTC is:

$$Z = \Delta\tilde{P}/\Delta\tilde{\tilde{U}} \tag{40}$$

The angle between pressure and volume flow rate shown in Fig. 2 becomes:

$$\alpha = \arctan\left(\frac{\|Im[Z]\|}{\|Re[Z]\|}\right) \tag{41}$$

Thus, the angle between the pressure and the displacement of the piston shown in Fig. 2 is:

$$\varphi = \frac{\pi}{2} - \alpha \tag{42}$$

For a dual-opposed linear compressor, the amplitude of the volume flow rate is given by (Lewis et al., 2006):

$$\left|\Delta\tilde{\tilde{U}}\right| = 2\omega X A_p \tag{43}$$

Based on Eq. (43), the thermodynamic characteristics of the working gas in the compression space can be adjusted accordingly with the stroke of the piston.

3.6. Cooling capacity

Under ideal conditions, the regenerator does not produce any thermal loss, and thus the PV power at the cold end of the regenerator will be completely used to generate the cooling effect. The time-averaged PV power at the cold end of the regenerator is then given by:

$$\left\langle \dot{W}_{pv,2} \right\rangle = \left| \frac{1}{\tau} \int_0^\tau \Delta \widetilde{P}_2 \Delta \widetilde{\dot{U}}_2 dt \right| = \frac{1}{2} \left| \Delta \widetilde{P}_2 \Delta \widetilde{\dot{U}}_2 \right| \tag{44}$$

However, in practice, the ineffectiveness of the regenerator has an effect on the cooling performance (Ko and Jeong, 2008; Razani et al., 2010; Tan and Dang, 2015). The time-averaged ineffectiveness loss of the regenerator $\langle \dot{Q}_{loss} \rangle$ is defined herein by (Razani et al., 2010):

$$\left\langle \dot{Q}_{loss} \right\rangle = \lambda C_p \left(\rho_1 T_1 \Delta \dot{U}_1 - \rho_2 T_2 \Delta \dot{U}_2 \right) \tag{45}$$

where λ is the ineffectiveness coefficient of the regenerator, and C_p is the specific heat at constant pressure.

Hence, the time-averaged cooling capacity of the SPTC is given by:

$$\left\langle \dot{Q}_c \right\rangle = \left\langle \dot{W}_{pv,2} \right\rangle - \left\langle \dot{Q}_{loss} \right\rangle \tag{46}$$

4. Thermodynamic performance of the linear compressor

Based on the above analyses, φ and ΔP can be calculated. According to Eqs. (13) and (14), the remaining two parameters, viz. θ and I, can be expressed as follows:

$$\theta = \operatorname{arccot}\left(\frac{k_m X + \Delta P A_p \cos\varphi - \omega^2 m X}{\omega c X + \Delta P A_p \sin\varphi} \right) \tag{47}$$

$$I = \frac{1}{BL} \sqrt{\left(\omega c X + \Delta P A_p \sin\varphi \right)^2 + \left(k_m X + \Delta P A_p \cos\varphi - \omega^2 m X \right)^2} \tag{48}$$

As a result, the thermodynamic performance of the linear compressor coupled with a pulse tube cold finger can be evaluated, including the input electric power, the PV power, the conversion efficiencies, and the cooling efficiency, etc., as discussed as follows.

4.1. Input electric power

The input voltage of the linear compressor is determined by the magnetic field intensity, the resistance, the inductance and the length of the wire in the coil, for which the governing equation is given by (Veprik et al., 2009):

$$u = Ri + L_e \frac{di}{dt} + BL \frac{dx}{dt} \tag{49}$$

The time-averaged input electric power of the linear compressor can be expressed as:

$$\begin{aligned} \left\langle \dot{W}_e \right\rangle &= \frac{1}{2} I^2 R + \frac{1}{2} \omega BLIX \sin\theta \\ &= \frac{1}{2} I^2 R + \frac{1}{2} \omega X \left(\omega c X + \Delta P A_p \sin\varphi \right) \end{aligned} \tag{50}$$

According to Eq. (50), the time-averaged input electric power consists of the Joule loss of the coils and the output motor power. The inductance of the coil only affects the input voltage, but not the input electric power.

4.2. PV power

The PV power represents the actual output capacity of the linear compressor, and the time-averaged PV power is given by:

$$\begin{aligned} \left\langle \dot{W}_{PV} \right\rangle &= \frac{1}{\tau} \oint (P - P_m) dV = \frac{1}{\tau} \int_0^\tau (P - P_m) A_p \frac{dx}{dt} dt \\ &= \frac{1}{2} \omega \Delta P A_p X \sin\varphi \end{aligned} \tag{51}$$

Compared with Eq. (50), Eq. (51) can be expressed as:

$$\left\langle \dot{W}_{pv} \right\rangle = \left\langle \dot{W}_e \right\rangle - \frac{1}{2} I^2 R - \frac{1}{2} \omega^2 c X^2 \tag{52}$$

So the power losses of the compressor mainly include the Joule loss and the mechanic damping loss. The time-averaged Joule loss and the damping loss are given by:

$$\begin{aligned} \left\langle \dot{Q}_h \right\rangle = I^2 R = \frac{R}{B^2 L^2} \Big[&\left(\omega c X + \Delta P A_p \sin\varphi \right)^2 \\ &+ \left(k_m X + \Delta P A_p \cos\varphi - \omega^2 m X \right)^2 \Big] \end{aligned} \tag{53}$$

$$\left\langle \dot{Q}_{DL} \right\rangle = \frac{1}{2} \omega^2 c X^2 \tag{54}$$

4.3. Conversion efficiencies of the linear compressor

The conversion efficiencies of the compressor include the ones from electrical to motor power and from electrical to PV power.

The conversion efficiency from electrical to motor power can be expressed by:

$$\begin{aligned} \eta_{motor} &= \frac{\left\langle \dot{W}_e \right\rangle - \left\langle \dot{Q}_h \right\rangle}{\left\langle \dot{W}_e \right\rangle} \\ &= \frac{\omega^2 c X^2 + \omega X \Delta P A_p \sin\varphi}{\frac{R}{B^2 L^2} \left[\left(\omega c X + \Delta P A_p \sin\varphi \right)^2 + \left(k_m X + \Delta P A_p \cos\varphi - \omega^2 m X \right)^2 \right] + \omega^2 c X^2 + \omega X \Delta P A_p \sin\varphi} \end{aligned} \tag{55}$$

Since the PV power can be determined by Eq. (51), the conversion efficiency from electrical to PV power is:

$$\begin{aligned} \eta_{PV} &= \frac{\left\langle \dot{W}_{PV} \right\rangle}{\left\langle \dot{W}_e \right\rangle} \\ &= \frac{\omega X \Delta P A_p \sin\varphi}{\frac{R}{B^2 L^2} \left[\left(\omega c X + \Delta P A_p \sin\varphi \right)^2 + \left(k_m X + \Delta P A_p \cos\varphi - \omega^2 m X \right)^2 \right] + \omega^2 c X^2 + \omega X \Delta P A_p \sin\varphi} \end{aligned} \tag{56}$$

4.4. Cooling efficiency of the SPTC

After the compressor is coupled with the cold finger, the cooling efficiency becomes an important parameter to evaluate the cooler performance. The relative Carnot efficiency, η_{Carnot}, is usually employed:

$$\eta_{Carnot} = \frac{COP}{COP_{Carnot}} = \frac{\left\langle \dot{Q}_c \right\rangle}{\left\langle \dot{W}_e \right\rangle} \frac{T_h - T_c}{T_c} \tag{57}$$

Table 1 – Geometrical parameters of the linear compressor.

Parameters	Values
Piston diameter	20 mm
Moving mass	200 g
Cylinder volume	7 cm^3
Magnet force coefficient (*BL*)	15 N/A
Wire resistance	3 Ω
Damping coefficient	4.5 N·s m^{-1}
Axial stiffness of flexure springs	4500 N/m

5. Systematic simulations on a specific case

In order to provide an elaborate explanation about the above theoretical analyses and the proposed model, the simulations based on a specific case will be given as follows.

Tables 1 and 2 show the geometrical parameters of a linear compressor and a pulse tube cold finger, respectively, which are representative in a series of compressors and cold fingers developed in the authors' laboratory. The 60 K, 80 K and 100 K are selected as the three typical cooling temperatures. The stroke of the piston, the charge pressure, and the reject temperature are set at 4 mm, 3.3 MPa, and 300 K, respectively. The designed frequency of the cold finger is 50 Hz at 80 K. The operating frequency of the SPTC will varies from 30 Hz to 100 Hz by a step of 5 Hz.

Table 2 – Geometrical parameters of the pulse tube cold finger.

Parameters	Values
Regenerator diameter	19.6 mm
Regenerator length	55.0 mm
Pulse tube diameter	11.2 mm
Pulse tube length	70.0 mm
Inertance tube I diameter	2.4 mm
Inertance tube I length	1500 mm
Inertance tube II diameter	5.8 mm
Inertance tube II length	3800 mm
Reservoir volume	400 cm^3

5.1. *Dynamic and thermodynamic characteristics of the linear compressor*

The variations of the four most important dynamic and thermodynamic parameters, viz. φ, ΔP, I and θ, will be simulated firstly.

Fig. 4 shows the variations of φ and θ with the operating frequency at different cooling temperatures, respectively. It is observed that φ changes dramatically with the increasing frequency, which indicates that the operating frequency has a significant effect on the phase angle. For example, while the frequency increases from 30 Hz to 65 Hz, the phase angle decreases sharply from about 100° to 35°. Therefore, the selection of the operating frequency should be limited in a narrow range in order to achieve the optimal phase angle for both cold finger and linear compressor. However, during the studied frequency range, at each specific frequency, when the cooling temperature increases from 60 K to 100 K, the variation of φ is less than 10°, which indicates that, compared with the operating frequency, the cooling temperature exerts a much less influence on φ. Similar to φ, the changes of θ are also dramatic and complicated with the increasing frequency, and at each specific frequency, the cooling temperature has a slight influence on θ. According to several previous studies (Dainez et al., 2014; Koh et al., 2002; Yuan et al., 1994), when θ equals 90°, the operating frequency will coincide with the resonance frequency of the linear compressor, thereby resulting in the minimum motor force shown in Fig. 2 and the maximum motor efficiency. It is found in Fig. 4 that the resonance frequencies occur at 50 Hz for 60 K, 45 Hz and 57 Hz for 80 K, and 40 Hz and 61 Hz for 100 K, respectively.

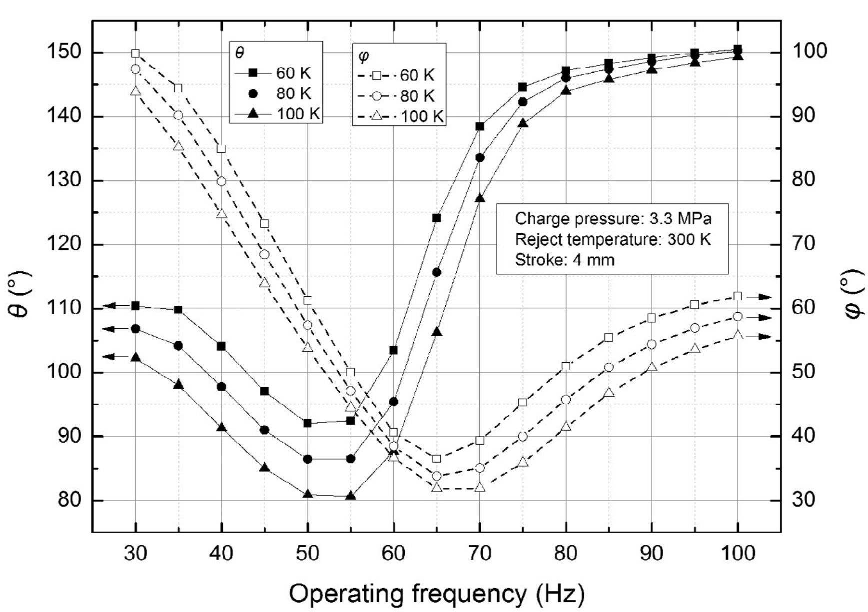

Fig. 4 – Variations of φ and θ with operating frequency at different cooling temperatures.

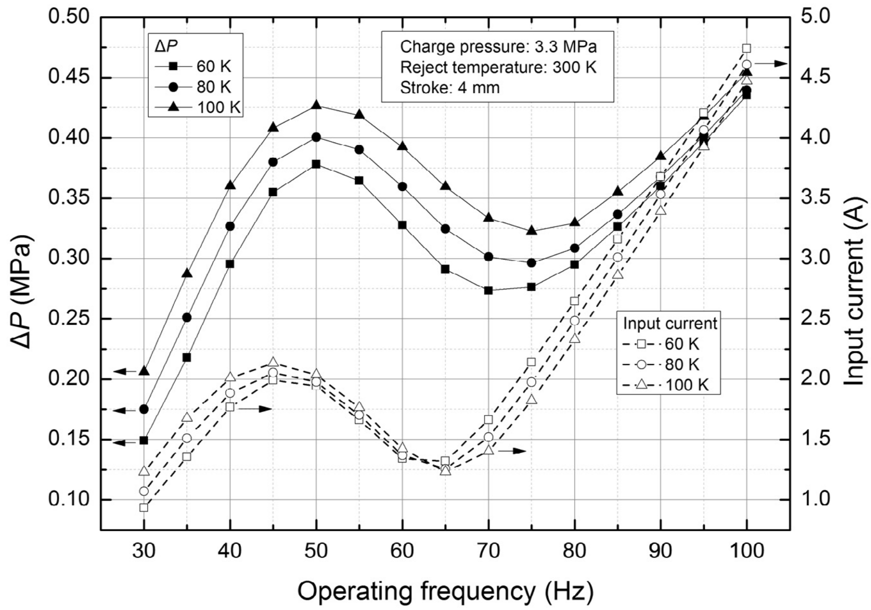

Fig. 5 – Variations of ΔP and *I* with operating frequency at different cooling temperatures.

Fig. 5 shows the variations of ΔP and *I* with the operating frequency at different cooling temperatures, respectively. ΔP increases sharply while the frequency changes from 30 Hz to 50 Hz. However, once larger than 50 Hz, the influence of the frequency on ΔP becomes smaller, and furthermore, ΔP even decreases slightly from 50 Hz to 75 Hz. And again, ΔP continues to increase sharply from 75 Hz to 100 Hz. An interesting phenomenon is that, in the whole range from 30 Hz to 100 Hz, at each specific frequency, ΔP only increases slightly as the cooling temperature changes from 60 K to 100 K, the maximum difference of which is about 0.06 MPa at 70 Hz. As the frequency increases, *I* changes dramatically, especially when larger than 65 Hz. Furthermore, the similarity between the curves shown in Fig. 5 indicates that *I* is generally determined by ΔP with the swept volume kept constant. At each specific frequency, if the cooling temperature increases from 60 K to 100 K, *I* increases between 30 Hz and 60 Hz, but decreases between 65 Hz and 100 Hz. Although the influence of the cooling temperature exerting on *I* seems to be complicated, the changes of *I* are all smaller than 0.3 A, and especially, between 45 Hz and 65 Hz, the changes actually can be neglected.

Based on the above analyses, it can be concluded that the operating frequency exerts important and complicated effects on the dynamic and thermodynamic characteristics of the linear compressor. By contrast, the influences exerted by the cooling temperature on these characteristics are much smaller, and in some cases can even be ignored.

5.2. *Thermodynamic performance of the linear compressor*

After φ, θ, ΔP and *I* are simulated, the thermodynamic performances of the compressor can be determined accordingly. Here we mainly discuss the PV power, the damping loss, the input electric power, the Joule loss, and the conversion efficiencies including η_{motor} and η_{pv}.

Fig. 6 shows the variations of the PV power and damping loss with the operating frequency at different cooling temperatures, respectively. When the frequency changes from 30 Hz to 100 Hz, the PV power increases from nearly zero to more than 300 W. Based on Eq. (51), the output PV power is mainly determined by ΔP, f, $\sin(\varphi)$ when the swept volume remains constant. According to Fig. 4, $\sin(\varphi)$ varies between 0.5 and 1, which is much smaller than the changes of the frequency or ΔP. Hence, the PV power is mainly affected by the operating frequency and ΔP. According to Fig. 6, a higher frequency can produce a larger PV power, which is one of the reasons why a smaller SPTC usually needs to operate at higher frequencies to make up for the weakness caused by the decrease of the swept volume. At each specific frequency, when the cooling temperature changes from 60 K to 100 K, the PV power also goes up due to the increase of ΔP. The maximum variation of the PV power caused by the cooling temperature is about 30 W, occurring at 65 Hz, with about 125 W for 60 K and 155 W for 100 K, respectively. The results indicate that the cooling temperature exerts a relatively strong influence on the PV power, and thus if the linear compressor is used to drive a SPTC working at a lower cooling temperature, it should be designed with a larger swept volume so that a big enough PV power can be available. The damping loss goes up monotonously with the increasing frequency. According to Eq. (54), the damping loss is only affected by the frequency, the stroke and the damping coefficient, but is independent of the cooling temperature. Therefore, only the variations at 80 K are shown in Fig. 6 to demonstrate the trends. Compared with the PV power, the damping loss is much smaller and thus can be neglected in most cases.

The variations of the input electric power and the Joule loss of the compressor with the operating frequency at different cooling temperatures can be determined based on Eqs. (50) and (53), respectively. As shown in Fig. 7, between 30 Hz and 70 Hz, the Joule loss varies within a limited scope and the electric

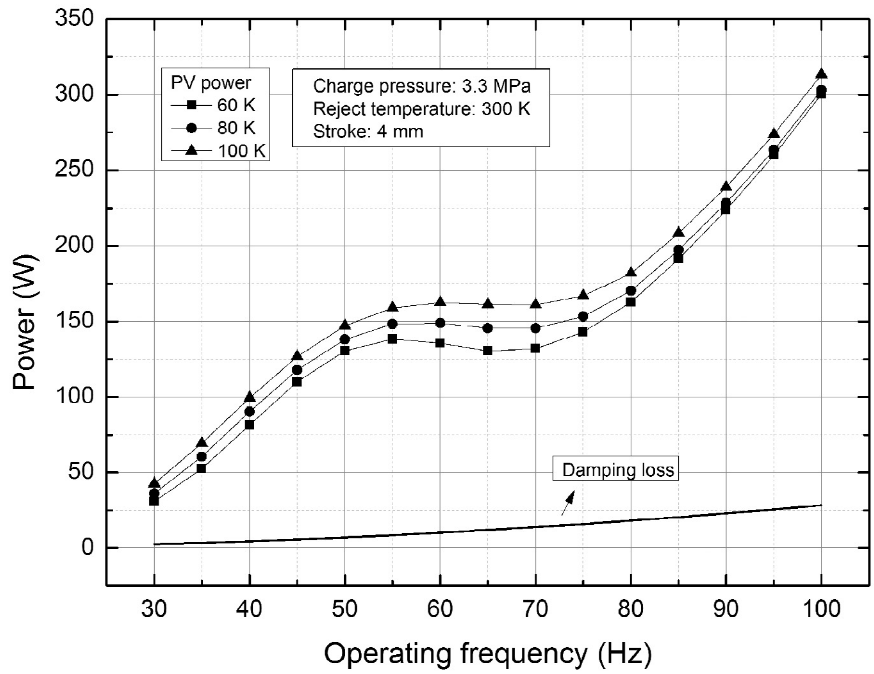

Fig. 6 – Variations of PV power and damping loss with operating frequency at different cooling temperatures.

power is mainly affected by the PV power. It indicates that when higher than 70 Hz, the Joule loss increases sharply and starts to account for a larger percentage of the electric power. But for each specific frequency, when the cooling temperature varies, the variation of the Joule loss is not obvious and thus the electric power is only influenced slightly.

Fig. 8 shows the variations of η_{motor} and η_{pv} with the operating frequency at three different cooling temperatures. According to the results, each curve has two peaks, which means that the compressor has two optimal frequencies at each cooling temperature. At either 80 K or 100 K, a higher optimal motor efficiency of over 90% is achieved at 65 Hz, which is about 4 Hz and 8 Hz larger than the corresponding resonance frequencies discussed in Section 5.1, respectively. By contrast, at 60 K, the motor efficiencies at 60 and 65 Hz are nearly equal, which means the optimal efficiency at 60 K is between 60 Hz and 65 Hz, with a difference of over 10 Hz from the resonance frequency given in Section 5.1. The above results show that the maximum motor efficiency of this compressor does not occur at its resonance frequency, different from the analyses in previous relevant studies (Dainez et al., 2014; Koh et al., 2002; Yuan et al., 1994). Our explanation is that, in the previous relevant studies, the optimal frequency was discussed with all of the other dynamic and thermodynamic characteristics,

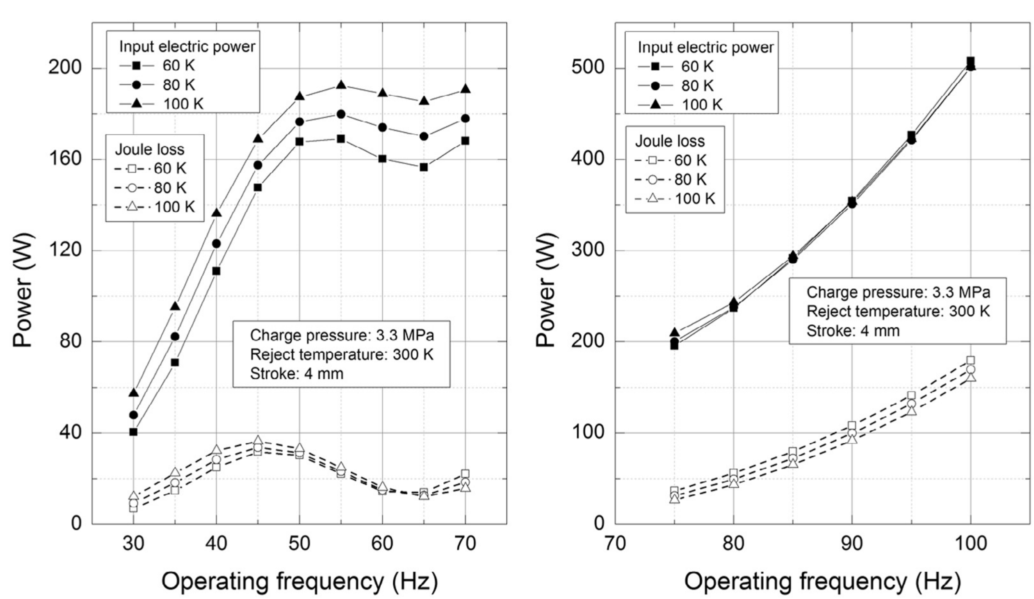

Fig. 7 – Variations of input electric power and Joule loss with operating frequency.

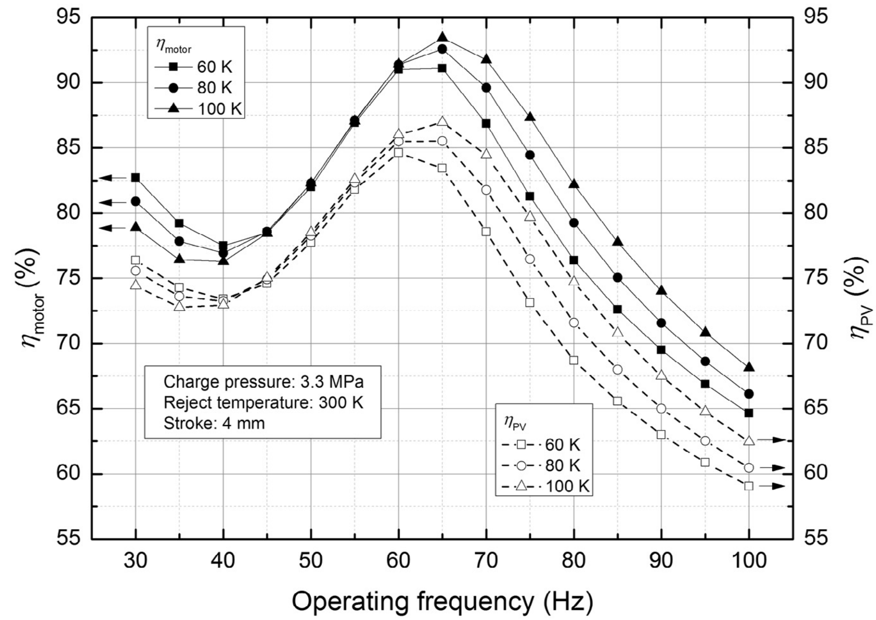

Fig. 8 – Variations of η_{motor} and η_{PV} with operating frequency at different cooling temperatures.

especially φ and ΔP, kept constant. However, when the cold finger is considered, the above characteristics cannot always remain constant with the varying frequency. As a result, the variations of η_{motor} with the frequency become considerably complicated and thus result in that the optimal frequency of the SPTC may not coincide with the resonance frequency. According to the simulation results, the cooling temperature only has a slight influence on η_{motor}, especially between 45 Hz and 60 Hz, which indicates that a well-designed linear compressor can perform efficiently while the cooling temperature varies in a considerably wide range, at least in the discussed range of 60 K to 100 K. The changing tendencies of η_{pv} are similar to those of η_{motor}, and the values of η_{pv} are also comparable to those shown in Fig. 8. The results indicate that the damping loss only exerts a slight influence on the electric power, and in some cases, the damping loss can be neglected in order to simplify the theoretical analyses.

5.3. *Cooling performance of the SPTC*

The cooling performances of the SPTC, mainly referring to the cooling capacity and η_{Carnot}, are the key parameters to evaluate the ability of the SPTC.

Fig. 9 shows the variations of the cooling capacity with the operating frequency at three cooling temperatures. Compared with the results in Fig. 6, the changing trends of the cooling capacity shown here are distinctly different from those of the PV power. The results indicate again that the operating frequency has an important and complicated effect on the thermodynamic characteristics of a SPTC. In Fig. 9, when the frequency is at around 50 Hz, the maximum cooling capacities of the three cooling temperatures are all achieved, with 19.1 W at 100 K, 12.4 W at 80 K, and 6.0 W at 60 K, respectively, which indicates that, for the same SPTC, there exists an optimal frequency in achieving the maximum cooling capacities in a wide range of cooling temperatures, or in other words, in a wide temperature range, the cooling temperature only has a slight influence on the optimal operating frequency.

Fig. 10 shows the variations of η_{Carnot} with the operating frequency at three cooling temperatures. The achieved optimal values of η_{Carnot} are 19.7% at 100 K, 18.2% at 80 K, and 13.6% at 60 K, respectively, and the corresponding frequencies are 45 Hz, 50 Hz, and 50 Hz, respectively. As mentioned above, the designed operating frequency of the cold finger is 50 Hz at 80 K. The results indicate that the optimal frequencies at both 60 K and 100 K are also around 50 Hz. However, the optimal frequencies of the motor efficiency discussed in Section 5.2 are around 65 Hz, about 15–20 Hz different from the optimal frequencies for η_{Carnot}. Since the cooling efficiency is one of the most important parameters to evaluate the whole SPTC, in practice, the actual optimal frequency of the SPTC often should coincide with the frequency for η_{Carnot}, which means that sometimes sacrifices might be made about the motor efficiency in an actual compromise, and the cold finger often exerts a greater influence on the optimal operating frequency of the whole SPTC than the linear compressor.

5.4. *Effects of compressor geometrical parameters on motor efficiency*

In this section, the effects of some important geometrical parameters of the compressor, such as the piston diameter, the moving mass, the magnet force coefficient, and the axial stiffness of the flexure springs, on the motor efficiency, will be investigated in consideration of the thermodynamic characteristics of the cold finger.

Fig. 11 shows the effect of the piston diameter on η_{motor} with the remaining parameters in Table 1 kept constant while the swept volume is kept at 5 cm^3 to fix the volume flow rate at each frequency. According to the results, at the cooling temperature of 80 K, with the piston diameter increasing from 9 mm

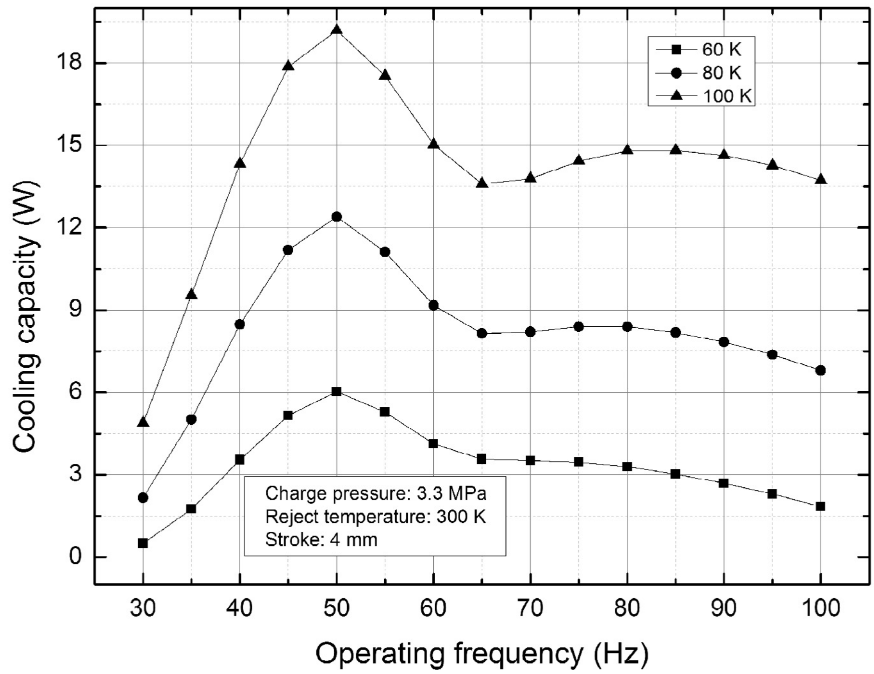

Fig. 9 – Variations of cooling capacity with operating frequency at different cooling temperatures.

to 11 mm, the optimal frequencies are achieved at 60 Hz, 65 Hz and 70 Hz, respectively. The corresponding motor efficiencies are 88%, 90% and 89%, respectively, merely varying slightly. Therefore, to adjust the piston diameter would be an effective approach to change the optimal operating frequency with η_{motor} remaining nearly unchanged.

Fig. 12 shows the effect of the moving mass on η_{motor} with the rest of the parameters in Table 1 kept constant. According to the results, the optimal frequency increases from 60 Hz to 70 Hz when the moving mass decreases from 300 g to 100 g. Therefore, a larger moving mass can lead to a lower optimal frequency, which is generally in accord with the results of the previous studies (Koh et al., 2002; Yuan et al., 1994). However, it is also found by the simulations that η_{motor} also decreases sharply with the increasing moving mass. Therefore, when the moving mass increases, the remaining parameters also should be adjusted accordingly to ensure η_{motor} be comparable to the original value.

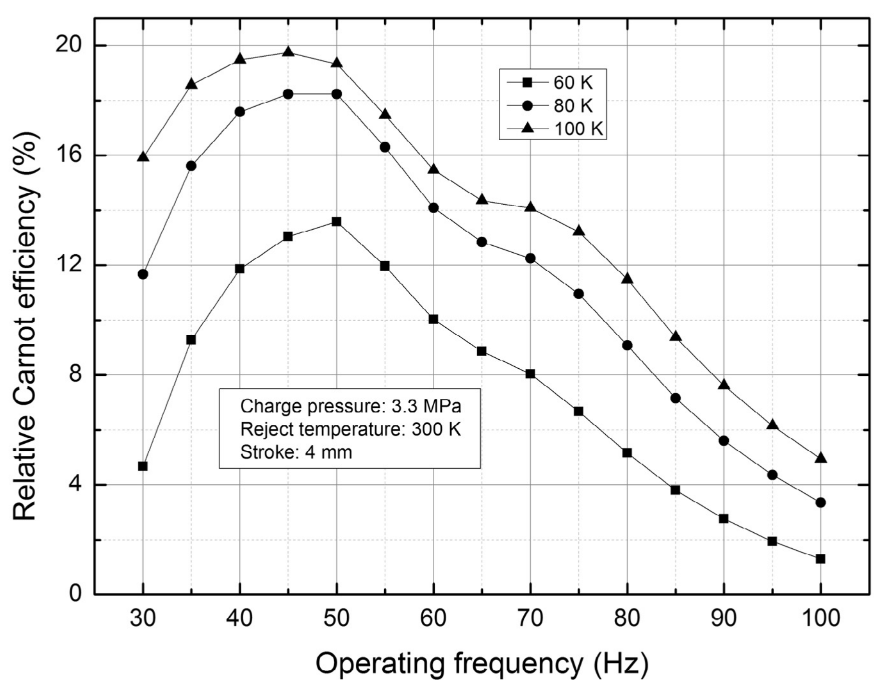

Fig. 10 – Variations of η_{Carnot} with operating frequency at different cooling temperatures.

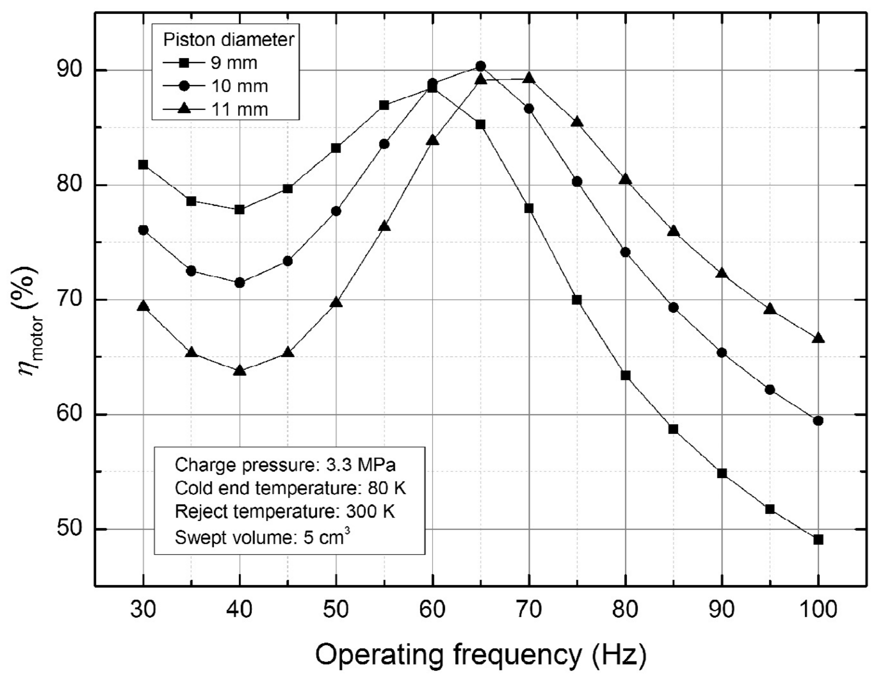

Fig. 11 – Effects of piston diameter on η_{motor}.

Fig. 13 shows the effect of the magnet force coefficient on η_{motor}. In this case, the magnetic field intensity is kept constant while only the wire length is adjusted. As a result, the resistance of the wire should change accordingly. As shown in Fig. 13, η_{motor} goes up as the magnet force coefficient increases from 10 N·s m^{-1} to 20 N·s m^{-1}, while the optimal frequency remains constant. The results indicate that to increase the magnet force coefficient is an effective approach to achieve a satisfactory η_{motor}. However, in practice, it is unfeasible to enhance the magnetic field intensity significantly due to the great difficulty in finding the appropriate magnetic materials with much higher energy products, and thus to increase the wire length becomes a better choice. However, a longer wire length will result in a larger moving mass. Therefore, if the wire length is adjusted, the masses of the other moving components should also be

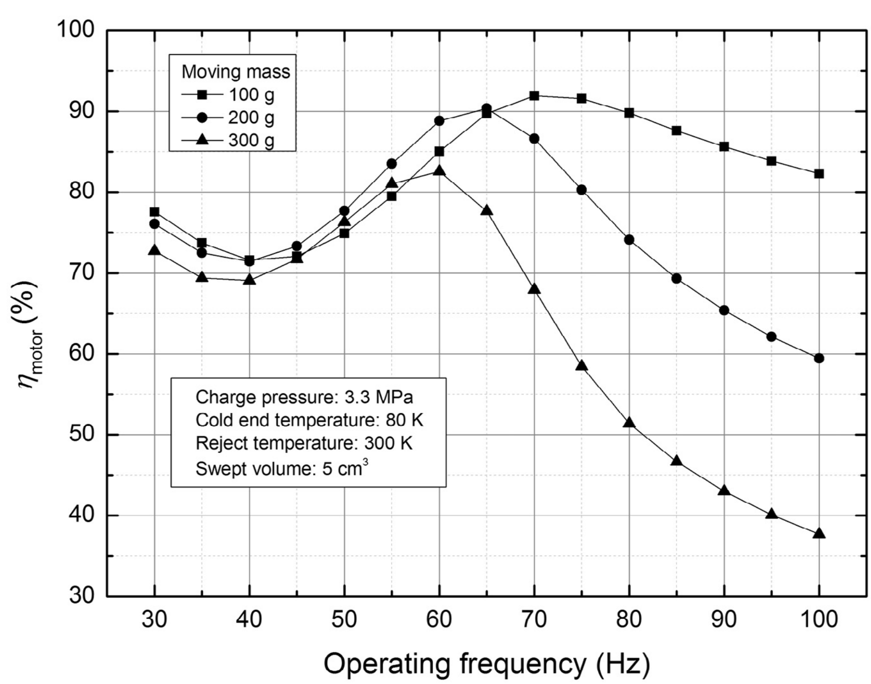

Fig. 12 – Effects of moving mass on η_{motor}.

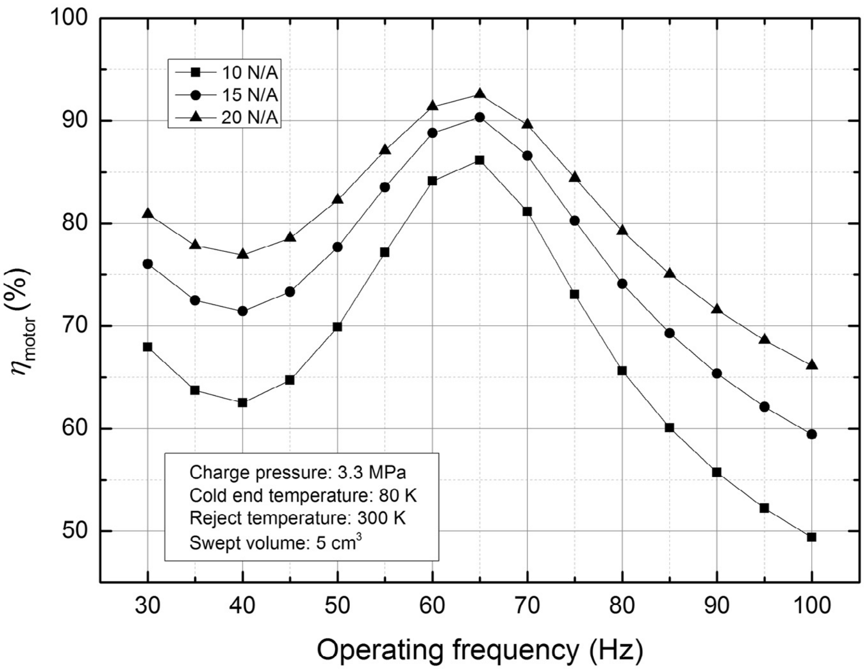

Fig. 13 – Effects of magnet force coefficient on η_{motor}.

adjusted accordingly to keep the overall moving mass unchanged.

Fig. 14 shows the effect of the axial stiffness of the flexure springs on the motor efficiency. As the axial stiffness changes from 1000 N/m to 8000 N/m, the optimal motor efficiency only increases about 3%, while the optimal frequency keeps unchanged. The results indicate that the axial stiffness of the flexure springs only has a slight influence on η_{motor}.

6. Conclusions

This paper has carried out systematic theoretical analyses and modeling of dynamic and thermodynamic characteristics of the moving-coil linear compressor in the inertance tube SPTC. The governing equations of these characteristics are deduced, and φ and ΔP are found to be the two key

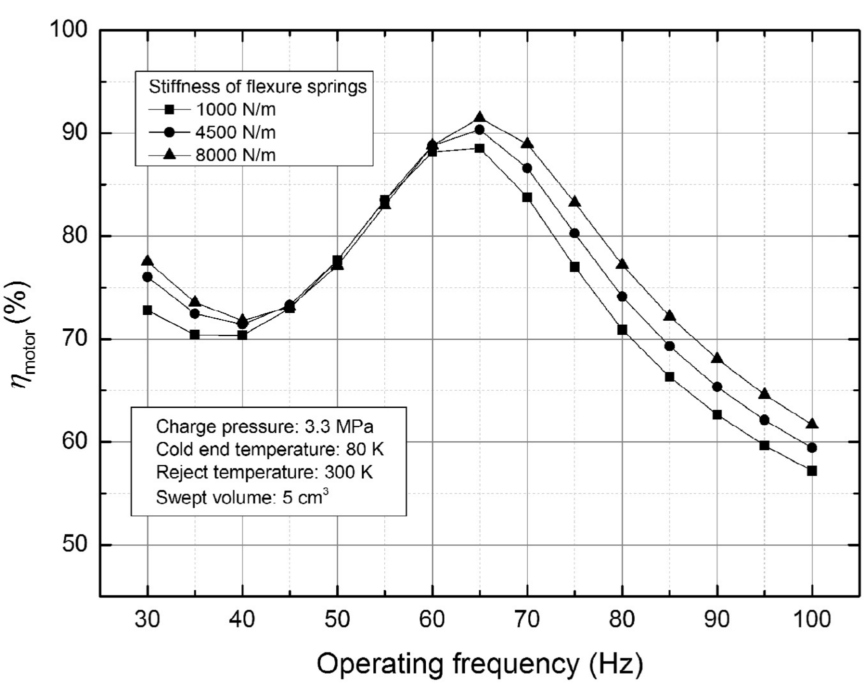

Fig. 14 – Effects of axial stiffness of flexure springs on η_{motor}.

parameters connecting the compressor to the pulse tube cold finger, which subsequently depend strongly on the thermodynamic characteristics of the cold finger. A further improved ECA model of the SPTC is developed to investigate the thermodynamic characteristics of the cold finger and their influences on φ and ΔP, which considers both the compression space and three heat exchangers, and the calculations start from the phase shifter to Warm HX II, and then to the inlets or exits of all the remaining components, with only one assumed parameter. φ, ΔP, I and θ can be determined in this way, and the effects of the cold finger on them can then be analyzed and evaluated.

The simulations on a specific case are given to provide elaborate explanations about the theoretical analyses and the proposed model with the operating frequency ranging from 30 Hz to 100 Hz at three typical cooling temperatures of 60 K, 80 K and 100 K.

Firstly, the variations of φ, ΔP, I and θ with the operating frequency at three cooling temperatures are simulated, respectively. The results indicate that the operating frequency exerts important and complicated effects on the characteristics of the compressor. By contrast, the influences of the cooling temperature on them are much smaller, and in some cases can even be ignored.

Subsequently, the variations of the thermodynamic performances of the compressor such as the PV power, the damping loss, the input electric power, the Joule loss, η_{motor} and η_{pv} with the operating frequency at the given cooling temperatures are simulated, respectively. The results indicate that the PV power is mainly affected by the operating frequency and ΔP, and at each specific frequency, the cooling temperature exerts a relatively strong influence on the PV power, and larger swept volumes of the compressor are needed if the driven SPTC work at lower cooling temperatures. The damping loss goes up monotonously with the increasing frequency but is independent of the cooling temperature. Between 30 Hz and 70 Hz, the Joule loss varies within a limited scope and the electric power is mainly affected by the PV power, whereas the Joule loss accounts for a larger percentage of the electric power at higher than 70 Hz. For each specific frequency, the electric power is only influenced slightly by the Joule loss when the cooling temperature varies. The effect of the operating frequency on η_{motor} is significant and considerably complicated, which may result in that the optimal frequency of the SPTC does not coincide with the resonance frequency. The cooling temperature only has a slight influence on η_{motor}, which indicates that a well-designed linear compressor can perform efficiently in a wide cooling temperature range. The changing tendencies of η_{pv} are similar to those of η_{motor}, and their values are also comparable, which indicates that the damping loss only exerts a slight influence on the electric power and can thus be neglected in many cases.

Furthermore, the variations of the SPTC cooling performances such as the cooling capacity and η_{Carnot} with the operating frequency at three cooling temperatures are simulated, respectively. The changing tendencies of the cooling capacity are distinctly different from those of the PV power, which indicates that the operating frequency has an important and complicated effect on the thermodynamic characteristics of a SPTC. In a wide temperature range, the cooling temperature only has a slight influence on the optimal operating frequency. The optimal η_{Carnot} at the three typical cooling temperatures are all achieved around the designed operating frequency of the cold finger, but are not consistent with the optimal frequencies for the motor efficiency, which means that in practice sacrifices might be made about the motor efficiency, and the cold finger often exerts a greater influence on the optimal frequency of the SPTC than the compressor.

Finally, the effects of geometrical parameters of the compressor, such as the piston diameter, the moving mass, the magnet force coefficient, and the axial stiffness of the flexure springs, on η_{motor} are simulated in consideration of the thermodynamic characteristics of the cold finger, respectively. It is found that to adjust the piston diameter is an effective approach to change the optimal operating frequency with η_{motor} kept constant. The optimal frequency is in inversely proportional to the moving mass, but η_{motor} also decreases sharply with the increasing moving mass. η_{motor} is in directly proportional to the magnet force coefficient, and in practice to increase the wire length is often a better choice than to enhance the magnetic field intensity. Moreover, the axial stiffness of the flexure springs only has a slight influence on η_{motor}.

The corresponding experimental verifications will be presented in Part B of this study (Dang et al., 2016).

Acknowledgments

This work is financially supported by The National Basic Research Program of China (No. 2013CB632802), The Chinese Academy of Sciences (No. XDA04060502) and The Science and Technology Commission of Shanghai Municipality (No. 15521104900).

Appendix A

According to Eqs. (30) and (31), the dynamic pressure and the volume flow rate can be expressed as follows:

$$\Delta\widetilde{P_x} = -\frac{C_1 e^{x\left(g-\sqrt{g^2+4r_g c_g}\right)/2}\left(\sqrt{g^2+4r_g c_g}+g\right)+C_2 e^{x\left(g+\sqrt{g^2+4r_g c_g}\right)/2}\left(g-\sqrt{g^2+4r_g c_g}\right)}{2c_g} \tag{A1}$$

$$\Delta\widetilde{\dot{U}_x} = C_1 e^{x\left(g-\sqrt{g^2+4r_g c_g}\right)/2} + C_2 e^{x\left(g+\sqrt{g^2+4r_g c_g}\right)/2} \tag{A2}$$

where C_1 and C_2 are expressed as follows:

$$C_1 = -\frac{2\Delta\widetilde{P_2}c_g + \Delta\widetilde{\dot{U}_1}\left(g-\sqrt{g^2+4r_g c_g}\right)}{2\sqrt{g^2+4r_g c_g}} \tag{A3}$$

$$C_2 = \frac{2\Delta\widetilde{P_2}c_g + \Delta\widetilde{\dot{U}_2}\left(\sqrt{g^2+4r_g c_g}+g\right)}{2\sqrt{g^2+4r_g c_g}} \tag{A4}$$

When x equals l_{reg}, the dynamic pressure $\Delta\widetilde{P_2}$ and the volume flow rate $\Delta\widetilde{\dot{U}_2}$ at the inlet of the regenerator can be determined.

REFERENCES

Bailey, P.B., Dadd, M.W., Hill, N., Cheuk, C.F., Raab, J., Tward, E., 2001. High performance flight cryocooler compressor. In: Cryocoolers 11. Kluwer Academic/Plenum Press, New York, pp. 169–174.

Bailey, P.B., Dadd, M.W., Stone, C.R., 2010–2011. Cool and straight: Linear compressors for refrigeration. In: Proc. Inst. Refrigeration, 4-1.

Bailly, Y., Nika, P., 2002. Comparison of two models of a double inlet miniature pulse tube refrigerator: part B electrical analogy. Cryogenics 42, 605–615.

Bradshaw, C.R., Groll, E.A., Garimella, S.V., 2011. A comprehensive model of a miniature-scale linear compressor for electronics cooling. Int. J. Refrigeration 34, 63–73.

Dainez, P.S., Oliveira, J., Nied, A., 2014. A linear resonant compressor model based on a new linearization method of the gas pressure force. Int. J. Refrigeration 48, 201–209.

Dang, H.Z., 2014. High efficiency pulse tube cryocoolers for aerospace applications. Adv. Cryog. Eng. 59, 378–385. AIP.

Dang, H.Z., 2015. Development of high performance moving-coil linear compressors for space Stirling-type pulse tube cryocoolers. Cryogenics 68, 1–18.

Dang, H.Z., Zhang, L., Tan, J., 2016. Dynamic and thermodynamic characteristics of the moving-coil linear compressor for the pulse tube cryocooler. Part B: experimental verifications. Int. J. Refrigeration 69, 497–504.

Davey, G., 1990. Review of the Oxford cryocooler. Adv. Cryog. Eng. 35, 1423–1430. Plenum Press, New York.

David, M., Marechal, J.C., 1995. Analytical model and experimental results of a miniature pulse tube refrigerator. In: Cryocooler 8. Plenum Press, New York, pp. 411–416.

Gaunekar, A.S., Narayankhedkar, K.G., Bapat, S.L., 1994. Dynamic and thermodynamic analysis of doubly motorized miniature Stirling cryocooler using double coil linear motor. Cryogenics 34, 43–50.

Heun, M.K., Collins, S.A., Johnson, D.L., Ross, R.G., Jr., 1997. Investigation of gas effects on cryocooler resonance characteristics. In: Cryocoolers 9. Plenum Press, New York, pp. 421–430.

Ki, T., Jeong, S., 2012. Step-by-step design methodology for efficient Stirling-type pulse tube refrigerator. Int. J. Refrigeration 35, 1166–1175.

Kim, H., Roh, C.G., Kim, J.K., Shin, J., Hwang, Y., Lee, J., 2009. An experimental and numerical study on dynamic characteristic of linear compressor in refrigeration system. Int. J. Refrigeration 32, 1536–1543.

Kim, J.K., Jeong, J.H., 2014. Dynamic response of a capacity-modulated linear compressor to supply voltage disturbances. Int. J. Refrigeration 40, 84–96.

Ko, J., Jeong, S., 2008. Analysis on the Stirling-type pulse tube refrigerator in consideration of dynamics of linear compressor. Cryogenics 48, 68–76.

Ko, J., Jeong, S., Kim, Y.K., 2008. Investigation on dynamic behavior of linear compressor in Stirling-type pulse tube refrigerator. Adv. Cryog. Eng. 53, 1093–1099. AIP.

Koh, D.Y., Hong, Y.J., Park, S.J., Kim, H.B., Lee, K.S., 2002. A study on the linear compressor characteristics of the Stirling cryocooler. Cryogenics 42, 427–432.

Lewis, M., Bradley, P., Radebaugh, R., 2006. Impedance measurements of inertance tubes. Adv. Cryog. Eng. 51, 1557–1563. AIP.

Liang, K., Stone, R., Hancock, W., Dadd, M., Bailey, P., 2014. Comparison between a crank-drive reciprocating compressor and a novel oil-free linear compressor. Int. J. Refrigeration 45, 25–34.

Magnusson, P.C., 1970, Boston. Transmission Lines and Ware Propagation.

Marquardt, E., Radebaugh, R., Kittel, P., 1993. Design equations and scaling laws for linear compressors with flexure springs. In: Cryocoolers 7. AFRL, Kirtland, pp. 783–804.

Nguyen, T.V., Raab, J., Durand, D., Tward, E., 2014. Small high cooling power space cooler. Adv. Cryog. Eng. 59, 365–370. AIP Publishing.

Nika, P., Bailly, Y., 2002. Comparison of two models of a double inlet miniature pulse tube refrigerator: part A thermodynamics. Cryogenics 42, 593–603.

Raab, J., Tward, E., 2010. Northrop Grumman aerospace systems cryocooler overview. Cryogenics 50, 572–581.

Razani, A., Fraser, T., Dodson, C., Roberts, T., 2010. Thermodynamic analysis and optimization based on exergy flow for a two-staged pulse tube refrigerator. Adv. Cryog. Eng. 55, 113–120. AIP.

Ross, R.G., Jr., 2007. Aerospace coolers: a 50-year quest for long life cryogenic cooling in space. In: Timmerhaus, K.D., Reed, R.P. (Eds.), Cryogenic Engineering: Fifty Years of Progress. Springer, New York, pp. 225–284.

Ross, R.G., Jr., Boyle, R.F., 2007. An overview of NASA space cryocooler programs—2006. In: Cryocoolers 14. ICC Press, Boulder, pp. 1–10.

Skilling, H.H., 1951. Electric Transmission Lines. McGraw-Hill, New York.

Storch, P.J., Radebaugh, R., Zimmerman, J.E., 1990. Analytical model for the refrigeration power of the orifice pulse tube refrigerator. National Institute of Standard and Technology, Boulder.

Swift, G.W., 2002. Themoacoustics: A Unifying Perspective for Some Engines and Refrigerators. Acoustical Society of America, Los Alamos, Sewickley, PA.

Tan, J., Dang, H.Z., 2015. An electrical circuit analogy model for analyses and optimizations of the Stirling-type pulse tube cryocooler. Cryogenics 71, 18–29.

Veprik, A., Nachman, I., Pundak, N., 2009. Dynamic counterbalancing the single-piston linear compressor of a Stirling cryogenic cooler. Cryogenics 49, 165–170.

Yuan, S.W.K., Naes, L.G., Nast, T.C., 1994. Prediction of natural frequency of the NASA 80 K cooler by the Stirling refrigerator performance model. Cryogenics 34, 383–388.